International Journal of Nanomedicine

Dovepress

open access to scientific and medical research

Open Access Full Text Article

ORIGINAL RESEARCH

An Oxygen-Sufficient Nanoplatform for Enhanced Imaging-Guided Microwave Dynamic Therapy Against Hypoxic Tumors

Rui Yang[1], Jiayan Huang[1], Min Liao[1], Jianbo Huang[1], Binyang Gao[1], Huan Zhang[1], Jie Zhou[1], Jinshun Xu[2], Qiang Lu[1]

[1]Department of Ultrasound, Laboratory of Ultrasound Medicine, West China Hospital of Sichuan University, Chengdu, Sichuan, 610041, People's Republic of China; [2]Ultrasound Medical Center, Sichuan Cancer Hospital & Institute, Sichuan Cancer Center, Cancer Hospital Affiliated to School of Medicine, University of Electronic Science and Technology of China, Chengdu, Sichuan, 610041, People's Republic of China

Correspondence: Qiang Lu, Department of Ultrasound, Laboratory of Ultrasound Medicine, West China Hospital of Sichuan University, Chengdu, Sichuan, 610041, People's Republic of China, Tel/Fax +86 13882175090, Email luqiang@scu.edu.cn; Jinshun Xu, Ultrasound Medical Center, Sichuan Cancer Hospital & Institute, Sichuan Cancer Center, Cancer Hospital Affiliated to School of Medicine, University of Electronic Science and Technology of China, Chengdu, Sichuan, 610041, People's Republic of China, Tel/Fax +86 18708491127, Email jsxu86@163.com

Background: Microwave dynamic therapy (MDT) as a novel reactive oxygen species (ROS)-based therapeutic modality has been explored as a promising modality for cancer treatment. However, the intrinsic hypoxic tumor microenvironment (TME) restricted the effectiveness of the MDT. The aim of this study is to develop an oxygen-sufficient nanoplatform with multi-modal imaging capability for enhanced MDT against hypoxic tumors.

Methods and Materials: The liquid perfluorocarbon-based nanoplatform PFP@IR780@O_2 was constructed by the phospholipid hydration and sonication method. Then, the characteristics, intracellular uptake process, and subcellular localization of PFP@IR780@O_2 were verified. Additionally, the abilities of ROS generation, the anti-hypoxia capability, multi-mode imaging capabilities, and MDT efficacy of the nanoplatform were evaluated via in vitro and in vivo experiments. Finally, the in vivo biocompatibility and toxicity were also evaluated.

Results: The prepared nanoparticles PFP@IR780@O_2 exhibited suitable size, improved stability, elevated dissolved oxygen level, enhanced cellular uptake, and mitochondria targeting capacity. Additionally, PFP@IR780@O_2 demonstrated in vitro and in vivo multimodal imaging capabilities involving ultrasound, fluorescence, and photoacoustic imaging. In vivo studies also indicated that nanoparticles were safe and capable of accumulating in the tumor site after intravenous injection. Furthermore, the PFP@IR780@O_2 nanoplatform mediated MDT could effectively alleviate the hypoxic TME, and elevate ROS concentration, thereby resulting in significant tumor growth inhibition.

Conclusion: Overall, the oxygen-sufficient nanoplatform with multi-bimodal imaging capability demonstrated improved MDT efficiency, indicating a promising strategy for treating hypoxic tumors.

Keywords: nanomedicine, perfluorocarbon, reactive oxygen species, tumor hypoxia relief

Introduction

Hepatocellular carcinoma (HCC) is the fourth most common malignant tumor worldwide with a five-year survival rate of just 18%.[1] The current treatments for HCC include resection, local treatment, targeted therapy, and immunotherapy. However, all the therapeutic options have ineluctable limitations, such as collateral damage to normal tissues, the poor killing of peripheral residual tumors, deficient curative outcomes, high recurrences, and low prognosis efficiency.[2,3] Therefore, new research is highly desirable to explore more efficient therapeutic strategies.

With remarkable advances in nanotechnology emerging, the reactive oxygen species (ROS)-based therapeutic nanoplatform has been explored as a promising and noninvasive modality for cancer treatment. Nevertheless, the earliest and most widely used strategy, photodynamic therapy (PDT), suffers from critical drawbacks such as poor light

Received: 23 August 2022
Accepted: 4 November 2022
Published: 21 November 2022

penetration depth and photo-toxicity.[4–6] Microwave dynamic therapy (MDT) is a novel ROS-based therapeutic modality that exploits microwave (MW) irradiation and sensitizers for tumor cells killing.[7–10] Compared to light, MW takes advantage of the deep penetrability, high controllability, and noninterference of bones and gases in the body, which makes the MDT a more suitable option for deep-seated tumor treatment.[7,8] Unfortunately, the effectiveness of the MDT is severely restricted by the intrinsic hypoxic tumor microenvironment (TME) as the tumor-dissolved oxygen is the main factor in the production of ROS.[11–13] Moreover, hypoxic TME is aggravated due to continuous oxygen consumption during the MDT procedure.[12,14] Therefore, supplying oxygen at tumor sites would be an effective strategy to achieve a satisfactory outcome for the MDT.

Up to now, multiple strategies have been designed to alleviate hypoxic TME.[14,15] One of the main methods is in situ oxygen generation by various hydrogen peroxide catalysts loaded in nanocarriers.[16–19] However, the effectiveness of this strategy is still greatly restricted by the limited amount of H_2O_2 available in the TME and the toxicity to normal cells of some metals. Another approach is tumor-targeted delivery of external oxygen by different nanocarriers. Hemoglobin, as one of the oxygen carriers, is commonly used to relieve tumor hypoxia, but it can result in severe side effects such as acute hypertension, acute nephrotoxicity, and even renal failure.[20] Apart from hemoglobin, perfluorocarbon (PFC) compounds have been widely explored as artificial blood substitutes and oxygen suppliers owing to their reliable biocompatibility and high oxygen solubility.[21–23] Recently, a work proposed that loading sensitizers into PFC nanodroplets could enhance the therapeutic outcome of PDT significantly.[24] Liu group also reported that a novel fluorocarbon-based nanoplatform can overcome the obstacle of hypoxic TME and reinforce ROS-based therapy against hypoxic solid tumor.[25] Moreover, the ROS lifetime in PFC is much longer than in the cellular environment or in water, which results in long-lasting ROS-based treatment effects.[24]

Based on the above background, we herein constructed a shell-core oxygen-sufficient liposomal nanoplatform to effectively relieve hypoxia, attenuate hypoxia-induced resistance to ROS-based MDT, and enhance MDT efficiency against highly aggressive HCC (Figure 1). Specifically, this elaborately designed nanoplatform PFP@IR780@O_2 was fabricated by loading perfluoropentane (PFP), a kind of PFC, as an oxygen reservoir and IR780 as sensitizer within liposomes. In addition, this nanoplatform could selectively accumulate at intracellular mitochondria endowed by the nature of IR780, achieving organelle-targeted MDT. Mitochondria, a vital organelle, is the main site of cellular ROS production (up to 90%) and the diffusion distance of ROS is extremely limited, mainly causing damage to the immediate vicinity of ROS generation.[26–29] Thus, the design of nanoplatforms targeting mitochondria could further amplify the

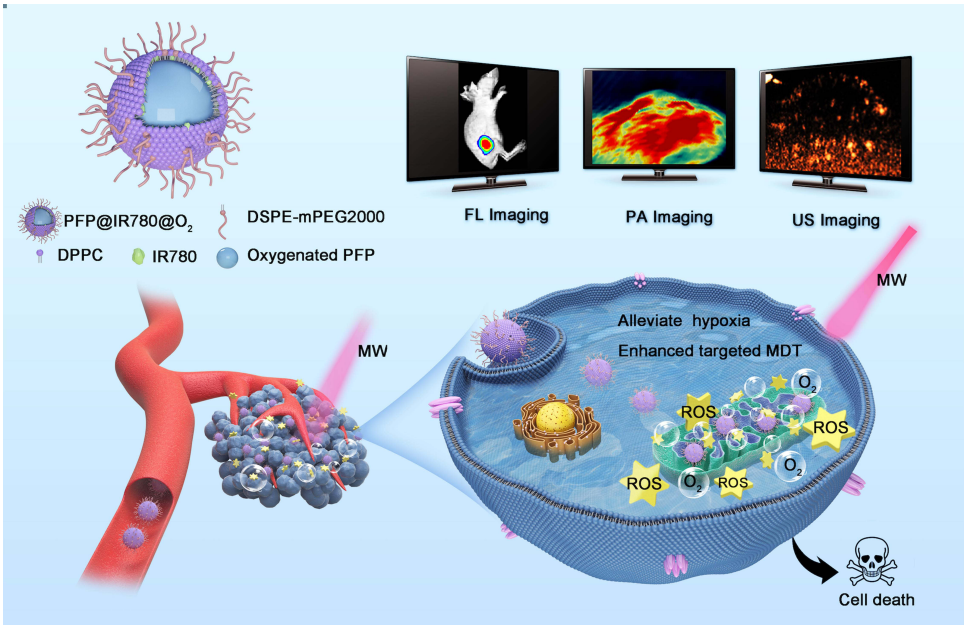

Figure 1 Schematic illustration of the multi-modal imaging-guided MDT with oxygenated PFP@IR780@O_2.

therapeutic effect of ROS-based MDT. Moreover, our group has previously achieved MW irradiation PFC liquid–gas-phase transition, inducing the ultrasound (US) imaging in vivo for monitoring the tumor accumulation of nanoparticles.[30] Therefore, the successfully prepared nanoplatforms could optimize therapeutic precision due to US imaging ability as well as fluorescence (FL) and photoacoustic (PA) imaging capabilities of IR780. As such, the as-developed PFP@IR780@O_2 nanoplatforms could not only greatly modulate hypoxic TME via the local MW-responsive oxygen release but also promote sufficient ROS generation near mitochondria under MW irradiation, further enhancing MDT efficiency against hypoxic HCC. In practice, both systematic in vitro and in vivo experiments were conducted to demonstrate the mitochondria-targeting MDT efficacy of the elaborately designed nanoplatforms.

Materials and Methods

Materials

DSPE-mPEG2000 was purchased from Xi'an Ruixi Biological Technology Co., Ltd. (China). 1,2-Dipalmitoyl-*sn*-glycerol-3-phosphocholine (DPPC), Cholesterol, PFP, IR780 were obtained from Sigma-Aldrich (St. Louis, MO, USA). Singlet Oxygen Sensor Green (SOSG) reagent, MitoTracker Green, and LysoTracker Green were obtained from Dalian Meilun Biotechnology Co., Ltd. (China). Reactive oxygen species assay kit was purchased from Beijing Solarbio Science and Technology Co., Ltd. (China). DiI, Hoechst 33342, calcein-AM/propidium iodide (PI) Kit was purchased from Suzhou Yuheng Biotechnology Co., Ltd. (China). Cell Counting (CCK8) was obtained from Boster Biological Technology Co., Ltd. (California, USA). All reagents used in this work were of analytical grade and were used without further purification.

Preparation of PFP-Encapsulated/IR780-Loaded Liposome

The liposomes loaded with IR780 and oxygen-enriched PFP (PFP@IR780@O_2) were prepared by an emulsion method adapted from previously published studies. First, the lipid compounds, DPPC, DSPE-mPEG2000, cholesterol, and IR780, were mixed (at a weight ratio of 12:4:4:1) and then dissolved in 5 mL dichloromethane. The solvent was removed from a 25-mL round flask by rotary evaporation at 55°C to form a lipid film. After the complete evaporation of $CHCl_3$, the film was peeled off after the addition of 5 mL phosphate-buffered saline (PBS). Then, 0.4 mL PFP bubbled with oxygen gas till saturation was added slowly to the above suspension and the mixture was sonicated in an ice bath by a sonicator (SCIENTZ-IID, Ningbo Scientz Biotechnology Co., Ltd., Zhejiang, China) at an intensity of 100 W for 5 min (pulse duration, 5 s; pulse interval, 5 s). The solution was then centrifuged at 4000 g for 5 min and the supernatant was discarded. The precipitate was washed by PBS until the supernatant was clarified. Finally, the washed precipitate was resuspended in 5 mL PBS enriched with oxygen and stored at 4°C for further use.

LIP@IR780@O_2 and PFP@Blank@O_2 were prepared similarly without PFP or IR780 addition procedure. All of the operations were kept on ice and in the dark to prevent evaporation of the PFP and decomposition of the IR780.

Characterization of the PFP@IR780@O_2

The morphology and structure of PFP@IR780@O_2 were characterized with transmission electron microscope (TEM, Tecnai G2 F30 S-TWIN, FEI Co., Ltd., Hillsboro, Oregon State, USA). Size distribution, surface zeta potential, and polydispersity index (PDI) of the droplets were determined by dynamic light scattering (DLS) using a Malvern Zeta sizer Nano ZS unit (Malvern Instruments, Worcestershire, UK) at room temperature. The evaluation of the stability of PFP@IR780@O_2 was checked for 1 week in PBS. On each day, the samples were collected to analyze the changes in particle sizes and polydispersity index. Each experiment was independently performed at least three times. The entrapment efficiency and the content of IR780 loaded in droplets were determined in triplicate by an ultraviolet-visible (UV–Vis) spectrophotometer (L5S, INESA, China). The supernatant of centrifugation and washing process was collected and the concentration of IR780 in the supernatant was quantified by measuring the absorbance at 780 nm and comparing the reading to a standard concentration curve of free IR780 in the same solvent. The entrapment efficiency and the loading capacity were calculated as follows:

$$\text{entrapment efficiency (\%)} = \frac{\text{IR780 used in formulation} - \text{IR780 in supernatant}}{\text{IR780 used in formulation}} \times 100\%$$

$$\text{loading capacity (\%)} = \frac{\text{IR780 used in formulation} - \text{IR780 in supernatant}}{\text{mass of nanoparticles}} \times 100\%$$

Measurement of O_2 Release from PFP@IR780@O_2 Triggered by MW

In vitro oxygen release with MW exposure of the oxygenated PFP-encapsulated nanodroplets was studied in the hypoxic aqueous solution. The oxygen partial pressure (pO_2) of the hypoxic solution was adjusted to the hypoxic condition (pO_2 = 4.0 mg/L) using nitrogen purge. The solutions were divided into the following groups: PFP@IR780@O_2, PFP@IR780, and LIP@IR780@O_2. One milliliter solution of each type was added to 10 mL hypoxic solution and the concentration of dissolved oxygen was monitored over 7 min using portable dissolved oxygen meter equipment. After 60s, microwave (1W/cm^2) is exposed for 180s and the dissolved oxygen data of each solution was recorded every 30s. The dissolved oxygen meter was calibrated in the air before the experiment, and all experiments were performed at a stable room temperature (25°C) and humidity conditions. The experiments were repeated in triplicate for each independent sample and then averaged.

Measurement of ROS Generation in a Cell-Free System

The ROS generation of the nanodroplets after MW activation was indicated by the fluorescent intensity of the oxidized SOSG. Briefly, 0.01 mL of 25 μM SOSG and 0.1 mL PFP@IR780@O_2 suspensions (1.0, 2.0, 4.0 and 8.0 μg/mL) were added to black 96-well plates. The solution was irradiated with microwave (1W/cm^2, 3 min) while being kept in the dark. After irradiation, ROS production was quantified by measuring the fluorescence intensity of the oxidized SOSG with a fluorescence microplate reader (BioTek, VT, USA; Ex = 504 nm, Em = 525 nm). As for other groups, only nanoparticles were replaced and other operations followed the procedures of the group MW+PFP@IR780@O_2. And the final IR780 concentration is 4 μg/mL. All operations were performed without light exposure, and the experiments for each group were run in triplicate.

Measurement of ROS Generation in Cell System

In addition to the SOSG assay, MW-triggered ROS generation in the cell model was further detected with the fluorescence indicator DCFH-DA. Hepa1-6 cells seeded in the CLSM-specific culture disks at a density of 2×10^5 cells per dish were cultured in hypoxic or normoxic conditions, ie, 2% O_2, 5% CO_2, and 93% N_2 at 37 °C for 24 h. Subsequently, six groups were set as follows: the blank or control group (without treatment), MW-only group, PFP@Blank@O_2 combined with MW irradiation (MW+PFP@Blank@O_2), LIP@IR780@O_2 combined with MW irradiation (MW+ LIP@IR780@O_2), PFP@IR780@O_2 only, and PFP@IR780@O_2 combined with MW irradiation (MW+PFP@IR780@O_2). The final concentration of IR780 was 4 μg/mL. It is worth noting that all cells in the six groups were first incubated with 1 mL of serum-free medium containing DCFH-DA (1:1000/10μM) for 30 min, followed by corresponding treatments in each group. After another 4 h incubation in a hypoxic incubator, the cells were washed once with PBS and fixed by 4% paraformaldehyde (PFA, 1 mL) for 10 min and labeled with 1mL Hoechst 33342 (1 mM) for 10 min. Finally, the cells were replaced with 1mL PBS. The level of intracellular ROS was evaluated by detecting the green fluorescent signal of DCF (lex = 488 nm, lem = 525 nm) with confocal laser scanning microscopy (Leica TCS SP2, Germany).

Intracellular Uptake and Subcellular Localization

The intracellular uptake process of PFP@IR780@O_2 was investigated by confocal laser scanning microscopy (CLSM) and flow cytometry. For CLSM observation, the Hepa1-6 cells were seeded in the CLSM-specific culture disks at a density of 2×10^5 cells per dish and incubated overnight. Then, the culture media were replaced by 1 mL of the cell membrane fluorescent probe DiI labeled PFP@IR780@O_2 nanodroplets (DiI-IR780 NDs) or DiI labeled nanodroplets without IR780 (DiI-NDs) as control. After co-incubation for 1 h, 2 h, 3h, and 4 h, the cells were rinsed with PBS and fixed with 4% 1 mL PFA for 5 min, and then the cells were stained by Hoechst 33342 for 20 min. For

the flow cytometry test, Hepa1-6 cells were seeded into 6-well plates at a density of 2×10^5 cells per well and allowed to adhere overnight. Then, the culture media were replaced by DiI-IR780 NDs and DiI-NDs. After varied co-incubation durations (1, 2, 3, and 4 h), the Hepa1-6 cells were collected by trypsin, and flow cytometry analysis was performed to evaluate the fluorescence intensity quantitatively.

To assess the mitochondria-targeting ability of PFP@IR780@O_2, mitochondrion, and lysosome selective fluorescence trackers were used as subcellular location markers. The subcellular localization was detected by CLSM. After 4 h co-incubation of Hepa1-6 cells with DiI-IR780 NDs and DiI-NDs, cells were washed with PBS three times. Next, cells were stained with Hoechst 33342 (20 min) and Mito-Tracker and Lyso-Tracker to label the mitochondria and lysosomes, respectively, for an hour. Finally, the subcellular localization was observed using CLSM.

Cytotoxicity Evaluation in the Cell System

To evaluate cytotoxicity in vitro, Hepa1-6 cells were seeded into 96-well plates at a density of 1×10^4 cells per well and cultured for 24 h under hypoxic or normoxic conditions and allowed to adhere overnight. After 24 h, the culture medium above was replaced and the cells were treated with PFP@IR780@O_2, PFP@Blank@O_2 and LIP@IR780@O_2 dispersed in DMEM with 10% FBS at different concentrations (IR780 concentration: 0, 1, 2, 4 and 8 μg/mL) for another 4h hermetical incubation, right after which the cells were irradiated with MW (1W/cm^2, 3 min). Then, the drugs were removed and a mixed solution consisting of serum-free culturing medium (100μL) and CCK-8 (10μL) was added to each well and incubated for an additional 4 h. Finally, the absorbance intensity was measured at 450 nm using the microplate reader (Thermo Scientific Varioskan Flash, USA) and the viable percentage was calculated. Cells without any drugs were used as a negative control and three independent experiments were repeated.

MDT Efficiency Evaluation in the Cell System

The MDT efficiency was further evaluated using the calcein-AM/PI live/dead fluorescence staining. Hepa1-6 cells were seeded into 6-well plates at a density of 2×10^5 cells per well and cultured for 24 h under hypoxic conditions. After the cells on the samples were treated according to the above procedures, the cells were washed with PBS three times and stained with propidium iodide (PI, dead cells, red fluorescence) and calcein-AM (CAM, live cells, green fluorescence) for fluorescence microscopy to distinguish the living and dead cells. Each sample was stained for 15 min in the absence of light and observed under a fluorescence microscope (Zeiss AX10, Oberkochen, Germany). PBS used for cell washing as well as DMEM cell culture media was deoxygenated via bubbling with nitrogen.

To assess the degree of apoptosis, flow cytometry using Annexin V-fluorescein isothiocyanate (FITC)/PI double staining was conducted. Briefly, cells were seeded in 6-well plates at a density of 2×10^5 cells per well and cultured overnight in a hypoxic incubator at 37 °C until they adhered. Six groups same as those in the cell live/dead fluorescence staining assay was set, ie, control, MDT only, PFP@IR780@O_2 only, MW+PFP@Blank@O_2, MW+LIP@IR780@O_2 and MW+PFP@IR780@O_2. After different treatments, the cells were harvested from 6-well plates, washed with PBS, and collected by centrifugation. Then the cells were stained with an Annexin V-FITC/PI apoptosis kit following the manufacturer's instructions. After incubation for 15 min at room temperature in the dark, flow cytometry was used to quantitatively determine the apoptotic stages.

Tumor Animal Model

Female nude mice aging 4–5 weeks with an average weight of 15g were purchased from Chengdu DaShuo Biological Technology Co., Ltd. and were maintained in accordance with the guidelines of the Institutional Animal Care and Use Committee (IACUC) of the West China Hospital, Sichuan University. All processes were in accordance with the Chinese Society of Laboratory Animals on animal welfare and approved by the Animal Use and Care Management Advisory Committee of West China Hospital of Sichuan University (Approval No. 2020242A). The nude mice were housed in a group of six under 12 hours of light and 12 hours of dark cycles and were fed with mice-specific food (Chengdu DaShuo Biological Technology Co., Ltd.) and tap water.

For the establishment of the subcutaneous tumor-bearing mouse model, 1×10^7 Hepa1-6 cells suspended in 100 μL of PBS were subcutaneously implanted in the lateral part of the right hind leg. Tumor size was measured every 2 days using

a slide caliper. Seven days later, the tumor volumes approached about 100 mm^3 before the experiments. The tumor volume calculation is as follows: $V=AB^2/2$ (where A and B represent the maximum and minimum diameters of the tumor, respectively). The temperature of the tumor was monitored in real-time using the infrared thermal mapping instrument (FLUKE 572–2, Hawk-IR International, Inc., Everett, WA, USA).

The orthotopic HCC model of mice was established by transplanting subcutaneous tumors into the liver of a new set of nude mice. Briefly, the fresh tumor tissues were removed from the subcutaneous site and were subdivided into 1 mm^3 piece, then washed and immersed in sterile PBS. The healthy recipient nude mice were anesthetized by intraperitoneal injection of pentobarbital solution (40 mg/kg), followed by abdominal routine disinfection and laparotomy. Then the left medial lobe of the liver was exposed and the tumor pieces were transplanted into the liver through a small hole using ophthalmological forceps. After hemostasis with sterile gauzes, the liver incision was sutured with 9–0 nylon surgical sutures with local disinfection. All experiments were performed under strict sterile conditions. After the operation, all mice were imaged using an ultrasound machine (iU22, Koninklijke Philips N.V., Eindhoven, NL) with a 15–7 linear array probe once every 3 days since day 5 post orthotopic liver transplantation. During the study, the focus depth and other settings remained constant. The orthotopic liver tumor volume was calculated with the following equation: $V=L\times W\times H/2$ (where L and W represent the length and width, respectively, measured in the horizontal plane, and H represents height, measured in the sagittal plane).

In addition, at the end of in vivo experiments, the mice were euthanized by cervical dislocation.

In vivo Tumor Accumulation and Imaging

The Hepa1-6 tumor model was established on Balb/C nude mice 10 days before assessment and PFP@IR780@O_2 (100 μL, 100 μg/mL IR780) was intravenously injected into the mice. For fluorescence imaging, mice were imaged before and 0.5, 4, 8, 24, and 48 h post-injection using an IVIS spectrum in vivo imaging system (PerkinElmer, Caliper Life Sciences, MA, USA; excitation = 740 nm, emission = 790 nm). To detect the biodistribution of PFP@IR780@O_2 at 24 h, the main organs and tumor tissues were removed for ex vivo fluorescence imaging.

For PA imaging, PFP@IR780@O_2 suspension was scanned at different wavelengths (650 to 900 nm) to detect the maximum absorbance. At pre-determined time points post-injection, PA images were acquired using a real-time multi-spectral photoacoustic tomography (MSOT in Vision 128, iThera Medical GmbH, Neuherberg, Germany).

To evaluate the MW-triggered US imaging ability due to liquid–gas conversion of PFP, the mice were tail vein injected with 100 μL PFP@IR780@O_2, LIP@IR780@O_2 (100 μg/mL IR780) and saline as a negative control, separately. At 24h post-injection, US images were obtained before and after MW irradiation (1 W/cm, 5 min) using an ultrasonic instrument (iU22, Koninklijke Philips N.V., Eindhoven, NL).

In vivo Monitoring of Hypoxic Tumor Conditions

To evaluate the tumor hypoxia conditions in HCC cancer xenografts models after different therapies, the mice were divided into six groups as follows: control, MW only, PFP@IR780@O_2 only, MW+PFP@Blank@O_2, MW+LIP@IR780@O_2 and MW +PFP@IR780@O_2. Photoacoustic imaging (PA) was conducted 24 h after tail vein injection of different agents using multi-spectral photoacoustic tomography (MSOT in Vision 128, iThera Medical GmbH, Neuherberg, Germany). The tumor oxygenation status was imaged in the Oxy-Hemo mode and the detection wavelength of deoxygenated hemoglobin (Hb) was 700 nm, while oxygenated hemoglobin (HbO_2) was 850 nm. For the ex vivo immunofluorescence staining of tumor hypoxia and ROS generation, the mice were sacrificed and tumors were excised for HIF-1a and ROS immunofluorescence assay. All PA data were reconstructed and analyzed using the MSOT system and the fluorescence intensity was analyzed using ImageJ software.

Antitumor Efficacy in vivo

The evaluation of antitumor efficacy was conducted using Hepa1-6 subcutaneous and orthotopic HCC mouse models. Hepa1-6 tumor-bearing mice were randomly divided into six groups including control, MW only, PFP@IR780@O_2 only, MW+PFP@Blank@O_2, MW+LIP@IR780@ O_2, and MW +PFP@IR780@O_2, six mice per group for the subcutaneous tumor model and three mice per group for the orthotopic tumor model, respectively. The tumor volume of the subcutaneous tumor model was about 150–200 mm^3, while that of the orthotopic tumor model was about 50–70 mm^3.

PBS (100 μL) was intravenously injected into the control and MW-only group, while the nude mice in other groups were administered with 100μL nanoparticles (100 μg/mL IR780) intravenously. At 24 h post-injection, mice were anesthetized with 3% (v/v) isoflurane and the MW treatment was performed (1W/cm^2, 5 min). For the orthotopic tumor model, MW exposure was conducted under the guidance of ultrasonography and the treatment cycle was twice. The mice were fed for 14 and 15 days respectively and the body weight and the tumor volume were measured according to the regular period. Survival analysis of the orthotopic tumor model was conducted by observing every mouse daily until death. For the subcutaneous tumor model, the mice were sacrificed after 14 days, tumors and major organs were dissected, washed with PBS and weighed, and then processed for routine the hematoxylin and eosin (H&E), terminal deoxynucleotidyl transferase dUTP nick end labeling (TUNEL), and proliferating cell nuclear antigen (PCNA) staining.

Biosafety Analysis of PFP@IR780@O_2

To evaluate the in vivo biocompatibility and toxicity of different treatments, major organs (heart, liver, spleen, lung, and kidney) were collected after therapy and these organs were fixed in 4% PFA solution at 4 °C and then were stained with H&E to observe the tissue morphology alterations. Furthermore, the mice blood was collected via extirpating with the eyes for hematological and biochemical assays. For hematology, routine tests include white blood cell (WBC), neutrophils (NEUT), red blood cell (RBC), hematocrit (HCT), hemoglobin (HGB), mean corpuscular volume (MCV), mean corpuscular hemoglobin (MCH), lymphocytes (Lymph) and platelet (PLT). As for biochemical analysis, the serological liver function was studied using alanine aminotransferase (ALT) and aspartate aminotransferase (AST), while the renal function was detected using blood urea nitrogen (BUN) and serum creatinine (Crea).

Statistical Analysis

The obtained data were presented as the mean±standard deviation (SD), and a statistical comparison between the two groups was performed by a two-tailed Student *t*-test. Differences were considered significant at *P < 0.05, **P < 0.01, ***P < 0.001 and ****P < 0.0001. All the statistical analyses were conducted using the GraphPad Prism software (version 6.0).

Results and Discussion

Preparation and Characterization of PFP@IR780@O_2

The nanoplatform PFP@IR780@O_2 was fabricated via a single-step emulsion method, in which lipophilic IR780 was incorporated into the lipid membrane (composed of DPPC, DSPE-mPEG2000, cholesterol), and PFP approved by the FDA as the oxygen reservoir was encapsulated in the core under sonication.

The successfully synthesized PFP@IR780@O_2 nanodroplets appeared as uniformly green, milky suspensions (Figure 2A). According to the DLS results, the mean diameter of the newly fabricated PFP@IR780@O_2 nanodroplets was 266.50 ± 9.44 nm (Figure 2B), whereas that of PFP@Blank@O_2 nanodroplets without IR780 was 210.61 ± 16.69 nm, which were suitable sizes of perfluorocarbon nanodroplets for substantial penetration into tumor tissues through the enhanced permeation and retention effect. In addition, the TEM (Figure 2C) observation also displayed the diameter of the PFP@IR780@O_2 nanodroplets to be approximately 250 nm and exhibited a typical spherical morphology. Comparing the surface zeta potential of nanodroplets before and after loading IR780, a positively charged molecule, a higher surface charge of PFP@IR780@O_2 nanodroplets was observed, about −19.4 ± 4.47mV (Figure S1). The size and zeta potential difference both indicate that IR780 was successfully loaded into the nanodroplets. Moreover, the stability of the nanoparticle is a crucial indicator to determine whether it could be used for in vivo injection. The results (Figure 2D) showed that there was no notable difference in the mean size and polydispersity index (PDI) of PFP@IR780@O_2 after storing at room temperature for 7 days, suggesting that prepared PFP@IR780@O_2 possessed outstanding stability. Furthermore, according to UV-vis spectra (Figure 2E), IR780 nanodroplets showed characteristic peaks of IR780, whereas no obvious absorption was detected for pristine nanodroplets, verifying the successful loaded of IR780. In addition, according to the standard curve of IR780 in the UV−vis spectrum, the encapsulation efficiency of IR780 in the PFP@IR780@O_2 was 55.06±0.20% and the loading capacity was 10.48±0.56%.

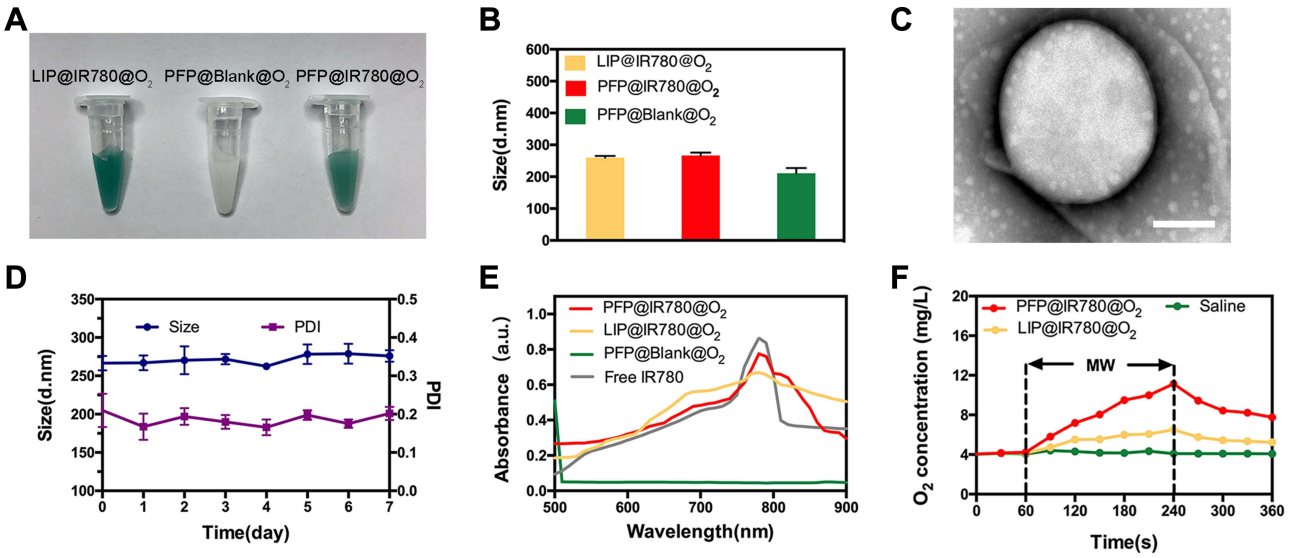

Figure 2 Characterizations of PFP@IR780@O_2 nanoparticles. (**A**) Photographs of LIP@IR780@O_2, PFP@Blank@O_2 and PFP@IR780@O_2 nanodroplets dispersed in PBS. (**B**) Size distribution of LIP@IR780@O_2, PFP@Blank@O_2 and PFP@IR780@O_2 nanodroplets as measured by DLS. (**C**) TEM image of PFP@IR780@O_2 nanodroplets (scale bar = 0.1μm). (**D**) The physical stability of PFP@IR780@O_2 determined over one week. (**E**) Absorbance spectra of free IR780, LIP@IR780@O_2, PFP@Blank@O_2 and PFP@IR780@O_2 as recorded by a UV–vis spectrophotometer. (**F**) MW-triggered O_2 generation of various solutions (1 W/cm^2, 3 min). Data are shown as mean ± SD. Experiments were repeated three times independently.

Measurement of O_2 Release from PFP@IR780@O_2 Triggered by MW

Owing to the high solubility of O_2 in perfluorocarbon, PFP@IR780@O_2 may act as a highly competent O_2 reservoir. In vitro oxygen release with MW exposure of the oxygenated nanodroplets with or without PFP loading was studied in the hypoxic aqueous solution. The dissolved oxygen concentrations in those solutions were monitored by a portable oxygen meter in real-time (Figure 2F). As expected, the concentration of dissolved O_2 for all sample solutions remained approximately unchanged within the first 60s after addition to deoxygenated water. When an external microwave (1W/cm^2) was applied to the solutions, sharply increased oxygen concentration was observed for PFP@IR780@O_2 solutions, while the solutions of LIP@IR780@O_2 nanodroplets exhibited no obvious increase in the level of dissolved O_2, confirming that MW could induce a burst release of O_2 dissolved in PFP. Hence, once PFP@IR780@O_2 arrives at the tumor site, the nanoparticles would gradually release O_2 into the surrounding hypoxic microenvironment upon MW irradiation, resulting in sufficient O_2 for the MDT effect.

Measurement of ROS Generation

As far as we know, MDT-induced cell damage was proposed to result from the overproduction of ROS which is associated with detrimental effects for cancer cells, including membrane and cytoskeletal damage, DNA fragmentation, loss of mitochondrial membrane potential, etc.[31] Thus, to identify the potential MDT efficiency of as-prepared nanodroplets, SOSG, a widely used ROS detection probe, was employed to analyze the ROS generation in vitro. In the presence of ROS, the oxidation of SOSG results in increased fluorescence and therefore provides a means of monitoring ROS production. An increase in SOSG fluorescence intensity was observed with increasing PFP@IR780@O_2 concentration (Figure 3A), attributed to the increased IR780 amount, indicating that ROS generation of PFP@IR780@O_2 was concentration-dependent. Furthermore, to explore whether oxygen supply would facilitate ROS generation, we measured the varying extent of fluorescence gain in hypoxic aqueous solution in the presence of PFP@IR780@O_2, LIP@IR780@O_2, and PFP@Blank@O_2 irradiated by MW (Figure 3B). The fluorescence intensity of PFP@IR780@O_2+MW was significantly higher than that of the LIP@IR780@O_2+MW group, indicating that O_2 dissolved in PFP is the main factor in the production of ROS. In contrast, no obvious fluorescence intensity increase was detected in the control, MW-only, or PFP@Blank@O_2+MW group, verifying IR780 could absorb MW energy and change oxygen into ROS.

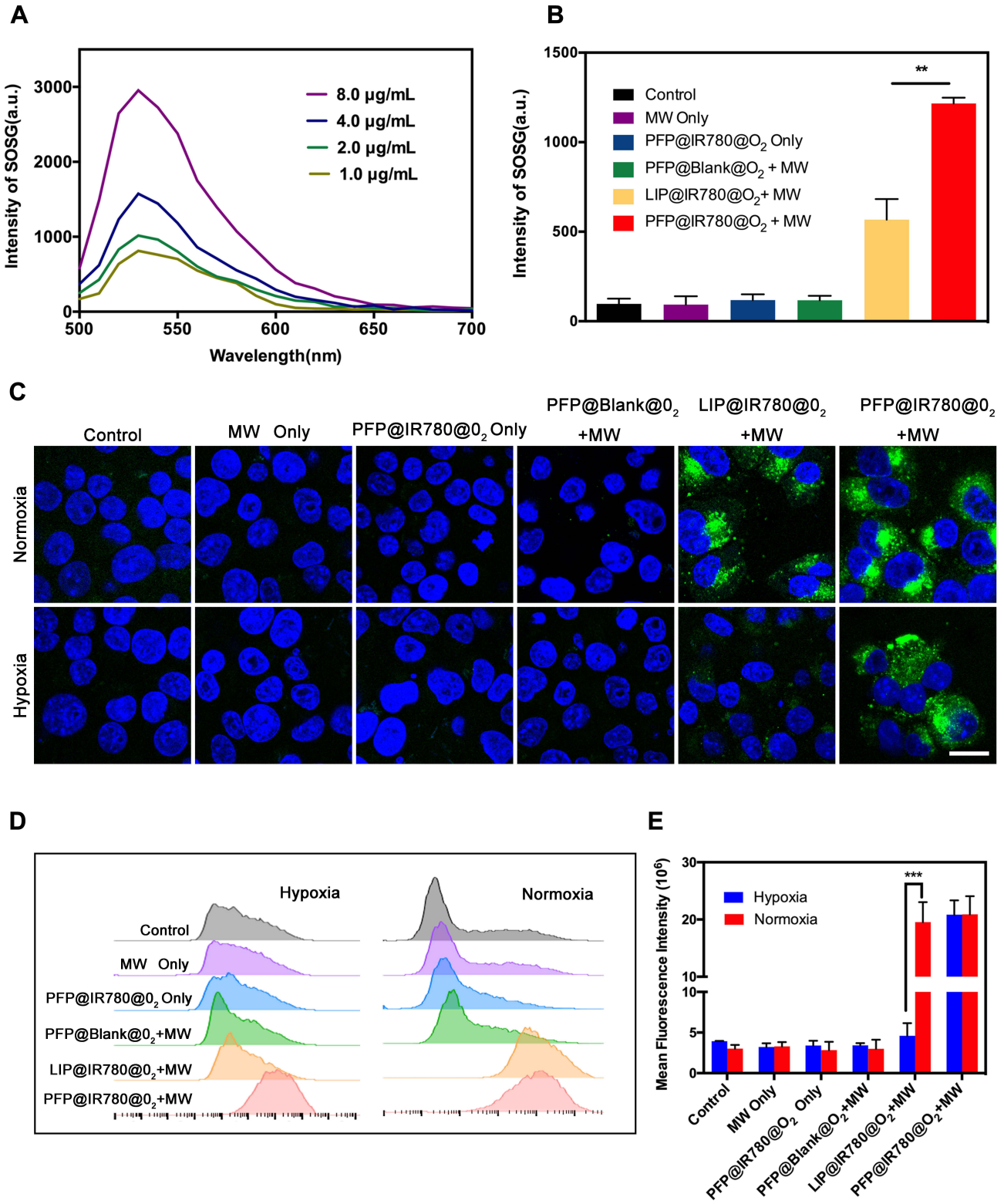

Figure 3 In vitro and intracellular ROS production. (**A**) Concentration-dependent ROS generation of PFP@IR780@O_2 upon MW irradiation (1 W/cm^2, 3 min). (**B**) In vitro comparisons of ROS production among six groups including control, MW only, PFP@IR780@O_2 only, PFP@Blank@O_2+MW, LIP@IR780@O_2+MW and PFP@IR780@O_2 +MW, as determined by the increase of the oxidation of SOSG fluorescence intensity. (**C**) Confocal images of Hepa1-6 cells exposed to different treatments at normoxic or hypoxic conditions, showing ROS generation detected by DCFH-DA and green fluorescence indicate positive staining for ROS. (**D**) Flow cytometry analysis of ROS generation at normoxic or hypoxic conditions. (**E**) Mean fluorescence intensities of ROS generation. Experiments were repeated three times independently. Data are shown as mean ± SD. **p<0.01, ***p<0.001. The scale bars are 20 μm.

After confirming oxygen released from PFP@IR780@O_2 would be favorable for MDT in a hypoxic aqueous solution, the intracellular ROS production was further evaluated with a ROS assay kit DCFH-DA (2′,7′-dichlorofluorescein diacetate), both in hypoxic and normoxic conditions. The DCFH-DA dye can be oxidized to DCF by the presence of ROS in cells, showing green fluorescence when excited at 520 nm. As expected, the control group without any treatment and MW or PFP@IR780@O_2-alone group showed no obvious green fluorescence, no matter the difference in oxygen levels of environments (Figure 3C). After the Hepa1-6 cells were treated with different nanodroplets and then exposed to MW, PFP@IR780@O_2 nanoparticles displayed a similar bright green fluorescence in both hypoxic and normoxic medium, whereas the fluorescence intensity of LIP@IR780@O_2 +MW group was decreased in the hypoxic condition. These results indicated that the ROS generation depended on the oxygen concentration during the MDT treatment and also suggested that our optimal nanoparticles could successfully enrich oxygen to maintain ROS production for keeping highly efficient MDT against a hypoxic tumor environment. In addition, we quantitatively analyzed ROS production by flow cytometry and found that the trend was consistent with CLSM results (Figure 3D and E).

Together with the aforementioned in vitro SOSG results, we conclude that PFP@IR780@O_2 can be used as an efficient MW dynamic agent and could enrich oxygen to accelerate ROS generation under MW irradiation to induce toxic ROS effects in tumor hypoxic conditions.

Intracellular Uptake and Mitochondria Targeting of PFP@IR780@O_2

The effective penetration and accumulation of PFP@IR780@O_2 in tumor tissue is the premise of an efficient therapeutic effect. Compared with normal tissues, nanoparticles are more likely to selectively accumulate in tumor sites because of the enhanced permeability and retention (EPR) effect of solid tumors.[32] Hence, the intracellular uptake of the cell membrane fluorescent probe DiI labeled PFP@IR780@O_2 nanodroplets (Dil-IR780 NDs) with prolonged incubation time (1, 2, 3, and 4 h) were visualized by CLSM images and quantified by flow cytometry. As expected, the CLSM images of Hepa1-6 tumor cells clearly showed gradually increased red fluorescence originating from Dil-IR780 NDs with the extension of incubation time (Figure 4A). Comparatively, in the absence of IR780, only a small amount of red fluorescence was observed, even after 4 hours of coincubation. The trend of fluorescence intensity enhancement detected by flow cytometry was similar to that of CLSM (Figures 4B and S2). These results indicate more intracellular uptake of PFP@IR780@O_2 with extended in vivo circulation time enables a more efficient MDT effect.

Furthermore, we speculated that PFP@IR780@O_2 could not only selectively accumulate in tumor cells but also can target mitochondria to enhance MDT efficiency. Because IR780, as a lipophilic cation, could specifically bind to mitochondria due to the higher mitochondrial membrane potential in tumor cells.[33,34] To identify our conjecture, mitochondrion- and lysosome-selective fluorescence probes were used to monitor and compare the subcellular localization of PFP@IR780@O_2. As depicted in Figure 4C, the red fluorescence of PFP@IR780@O_2 showed extremely similar localization to the green signal of mitochondria, but different from that of the lysosome. The Pearson correlation (PC) coefficient of MitoTracker was 0.82, while that of LysoTracker was only 0.37, indicating the mitochondrion targeting of PFP@IR780@O_2 in tumor cells. However, no obvious red fluorescence was observed in the mitochondrial region of pristine NDs without IR780 loading (Figure S3), which further verified the active role of IR780 contributing to the mitochondria-targeting. Based on these results, we considered that the mitochondrion-targeting MDT could be more effective because mitochondria were susceptible to ROS and the destruction of mitochondrial biological function could inhibit cell respiration, thus reducing oxygen consumption in hypoxic tumor cells.

Cytotoxicity Evaluation in vitro

In our work, we used mouse hepatoma Hepa1-6 cells to evaluate the cytotoxicity of as-prepared nanocomposites using a standard Cell Counting Kit-8 (CCK-8) assay. After incubation with the PFP@IR780@O_2 nanoparticles at different volume concentrations (IR780 concentration: 0, 1, 2, 4, and 8 μg/mL) for 24 h in hypoxia condition, no significant cell death was observed compared with the PFP@Blank@O_2 group and LIP@IR780@O_2 group (Figure 5A), indicating negligible cytotoxicity of nanodroplets alone to cells. However, upon irradiation with MW (1W/cm^2, 3min), a significant decrease in cell viability of group PFP@IR780@O_2 was observed, whereas MW exposure did not affect the cytotoxicity of group LIP@IR780@O_2 (Figure 5B), suggesting that the formation of dissolved oxygen by nanodroplets enhanced the

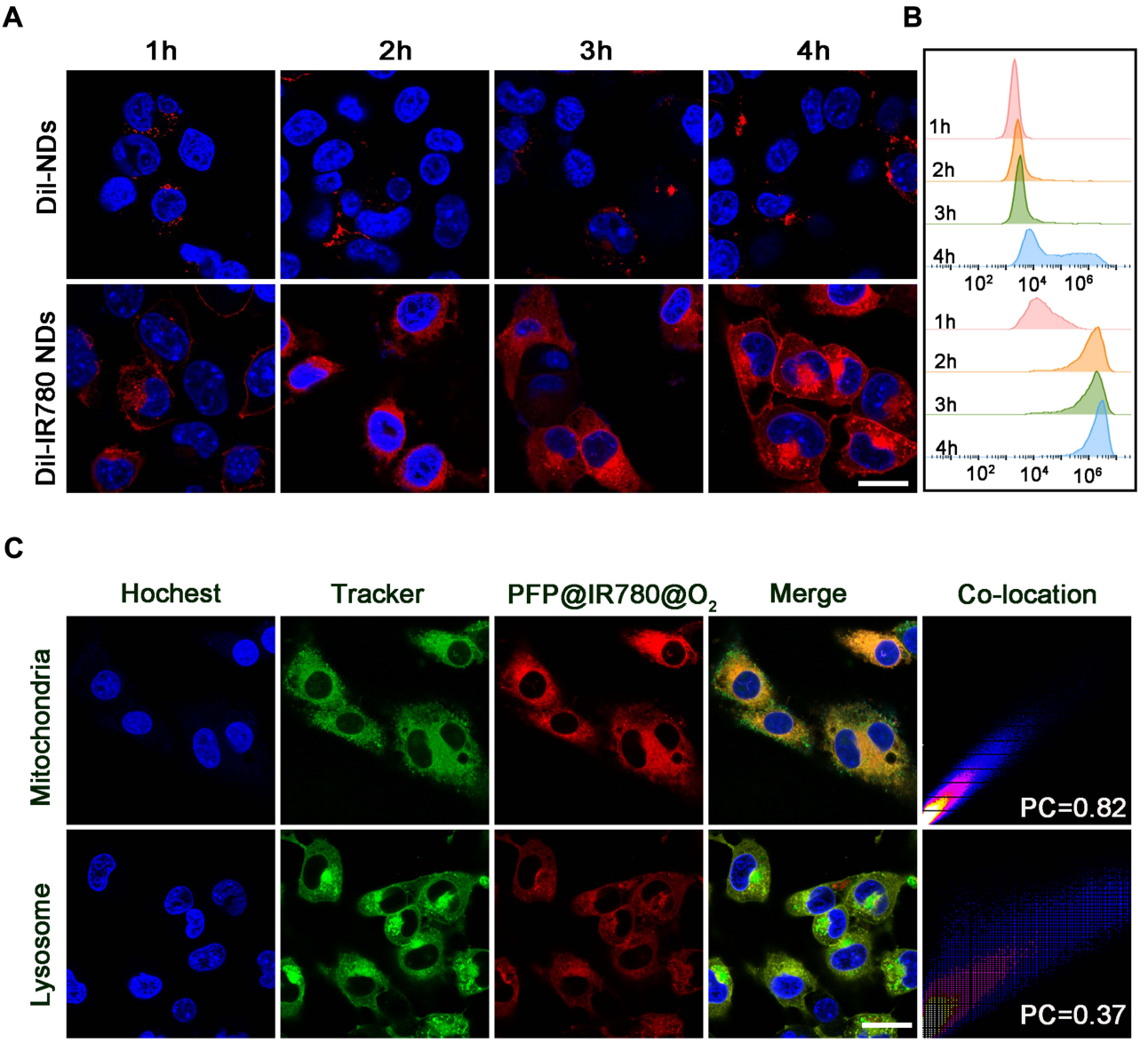

Figure 4 Intracellular uptake and mitochondrial targeting of PFP@IR780@O_2. (**A**) Intracellular uptake of DiI-NDs and DiI-IR780 NDs observed by confocal images after 1, 2, 3 and 4h coincubation with Hepa1-6 cells. (**B**) Representative flow cytometry analysis of intracellular uptake during various intervals of coincubation. (**C**) Subcellular localization of PFP@IR780@O_2 compared to mitochondria and lysosome trackers using CLSM. The scale bars are 20 μm.
Abbreviation: PC, Pearson correlation coefficient.

ROS generation at hypoxic atmosphere to enhance cell damage. Moreover, to further confirm that MDT efficiency is oxygen-dependent, 21% (normoxia) oxygen levels were also investigated. It was found that MW did not present much killing effect on blank cells regardless of oxygen levels (Figure 5B). Interestingly, LIP@IR780@O_2 nanoparticles displayed similar cytotoxicity to PFP@IR780@O_2 in the normoxic condition after MW exposure, while in the hypoxic condition, the cytotoxicity of group MW+ LIP@IR780@O_2 was significantly decreased. The reason may be that the normoxic condition could provide sufficient oxygen for group LIP@IR780@O_2 that MDT needed, which indicated that the ROS generation depended on the oxygen. Thus, it was expected that the PFP@IR780@O_2 would significantly enhance the MDT effect on anticancer in the hypoxic tumor environment.

MDT Efficiency Evaluation in vitro

The MDT efficiency in the hypoxic environment was further evaluated using the calcein-AM/PI Live/Dead fluorescence staining. The surviving cells with intact cell membrane and active intracellular esterase can trap the calcein inside, and

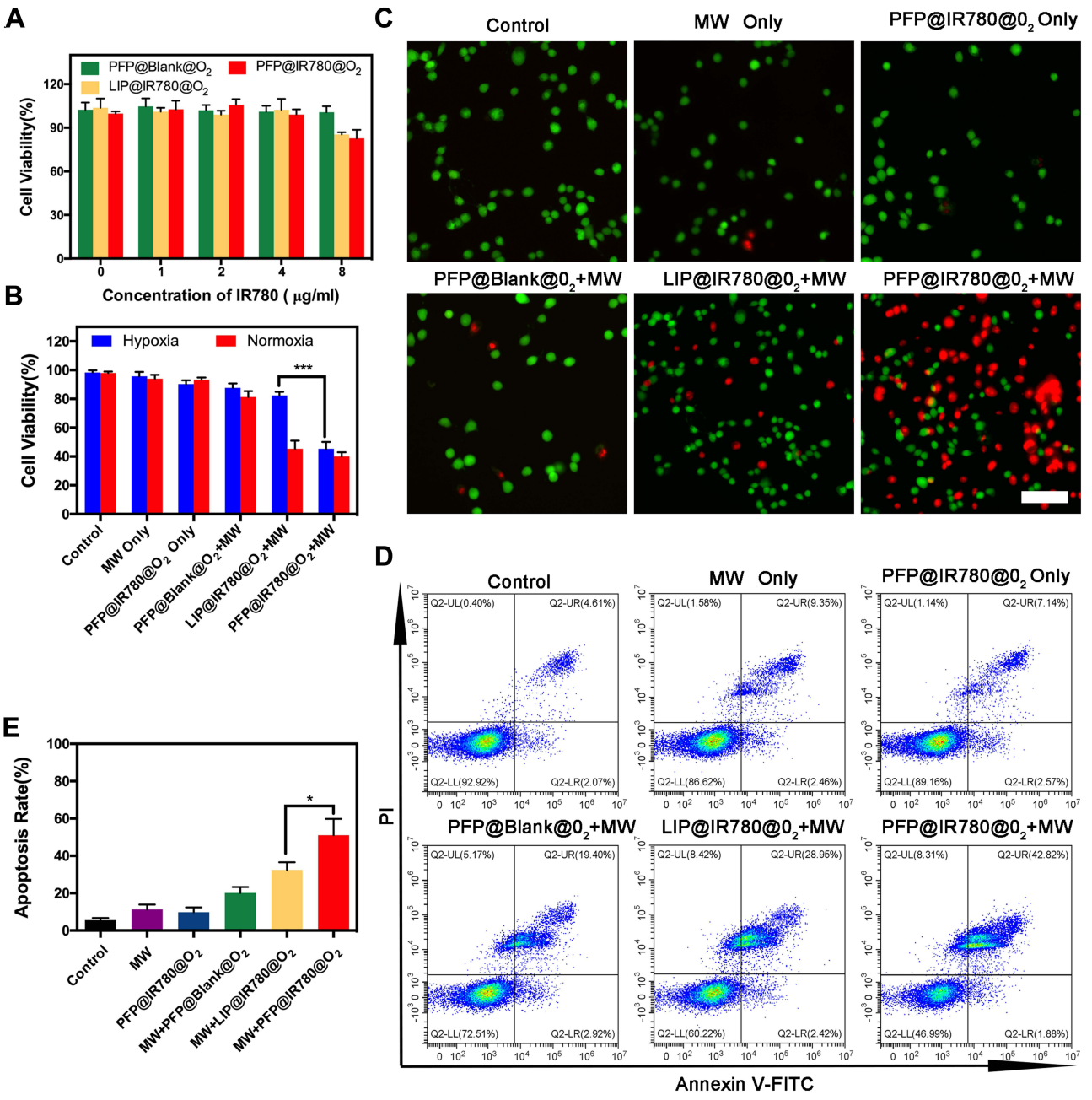

Figure 5 Cytotoxicity of nanoparticles and in vitro MDT of cancer cells in hypoxic conditions. (**A**) Viability of Hepa1-6 cells treated with various formulations at different concentrations in oxygen-deficient condition. (**B**) Cell viabilities of Hepa1-6 cells after different treatments in normoxia and hypoxia using CCK-8 kit. (**C**) Calcein-AM and PI co-stained fluorescence imaging of Hepa1-6 cells treated with varied probes after MW irradiation (1 W/cm^2, 3 min) in hypoxic condition. (**D**) Apoptosis of Hepa1-6 cells detected by flow cytometry after different treatments in hypoxic condition. (**E**) Quantitative analysis of the apoptosis rates by flow cytometry. Experiments were repeated three times independently. Data are shown as mean ± SD. *p < 0.05; ***p < 0.0001. The scale bars are 50 μm.

emit strong green fluorescence, while PI can only permeate into dead cells with no intact cell membrane and give out red fluorescence when combined with DNA. As presented in the fluorescent images (Figure 5C), in the control or PFP@IR780@O_2-alone-treated groups, many viable cells (green) were still visible, suggesting negligible damage effect from PFP@IR780@O_2-alone. Under the MW irradiation, a similar fluorescence distribution was observed in the PFP@Blank@O_2 and LIP@IR780@O_2-treated group, and a minimal number of dead cells (red) was observed. Meanwhile, almost all of the cells incubated with PFP@IR780@O_2 were killed and stained with red fluorescence after MW irradiation, indicating that the ROS generation to cause cell damage depended on the oxygen.

The improved anticancer activity of PFP@IR780@O_2 in the hypoxic environment was further assessed by determining the degree of apoptosis by flow cytometry using Annexin V-FITC/PI analysis as apoptosis is one of the mechanisms accounting for the anti-cancer activity. According to the results (Figure 5D and E), after treatment with PFP@IR780@O_2 in the hypoxic condition, the population of apoptotic or dead cells was 44.70% after irradiation (1W/cm^2, 3min), which was much higher than PFP@Blank@O_2 or LIP@IR780@O_2-treated groups. Moreover, in the control, MW-only or PFP@IR780@O_2-only group, negligible apoptotic or dead cells were found. The apoptosis results showed that PFP@IR780@O_2 could visibly induce apoptosis of cancer cells under hypoxic conditions.

The results of calcein-AM/PI co-staining imaging and flow cytometry analysis of apoptosis and necrosis agreed well with the data of the CCK-8 assay, confirming that ROS-mediated apoptosis could be severely suppressed in hypoxic regions of tumors due to the absence of sufficient oxygen content and PFP@IR780@O_2 nanoparticles upon MW irradiation could improve MDT efficiency in tumor hypoxic condition.

In vivo Biodistribution and Imaging

To determine whether PFP@IR780@O_2 could effectively accumulate in tumors for imaging and treatment, the inherent PA and FL imaging abilities of IR780 were employed to assess the in vivo biodistribution. After intravenous injection of PFP@IR780@O_2 in Hepa1-6 tumor-bearing mice, FL and PA images were acquired at different times (0, 0.5, 4, 8, 24, and 48 h), respectively (Figure 6A and B). Both signals gradually increased at the tumor site and the peak value was noted 24

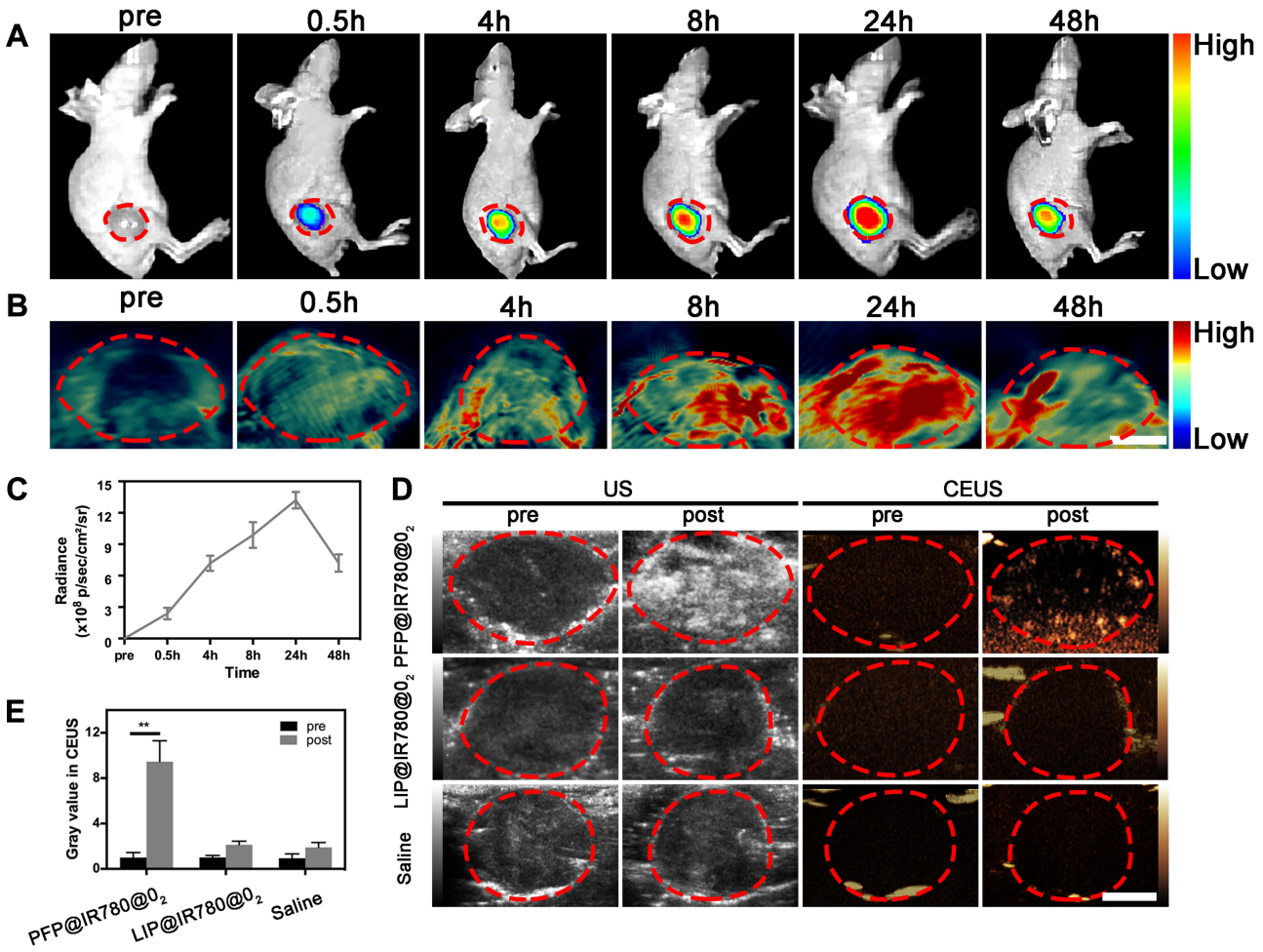

Figure 6 In vivo biodistribution and imaging. (**A**) Real-time fluorescence images of tumor-bearing mice before and after intravenous injection of PFP@IR780@O_2 at different time points. (**B**) In vivo PA images (λ= 780 nm) of tumor area before and after injection of PFP@IR780@O_2 at different time points. The scale bars are 50 mm. (**C**) The relative fluorescence intensities changing at the tumor site at the corresponding time points. (**D**) US (right) and CEUS (left) mode images of tumor-bearing mice at 24 h after tail vein injection of PFP@IR780@O_2, LIP@IR780@O_2 and saline, followed by MW irradiation (1 W/cm^2, 5 min). Red circles indicate tumor areas. (**E**) The gray values in CEUS mode of pre- and post-irradiation (n = 3). Data are shown as mean ± SD. **p < 0.01.

h post-injection (Figures 6C and S4), indicating the tumor-targeting ability of the PFP@IR780@O_2 via the EPR effect. To better characterize the biodistribution of PFP@IR780@O_2, tumors and main organs (heart, liver, spleen, lung, and kidneys) were collected after 24 h of intravenous injection for ex vivo fluorescence imaging. The strongest fluorescence was observed in the tumor tissue compared with other organs (Figure S5A). Besides, the fluorescence intensity of the nanodroplets in the lung was higher than that of the liver or kidney, and this was also observed in other PFC-related products.[35] Semi-quantification of the fluorescence signal intensity further confirmed these findings (Figure S5B). Both FL and PA imaging results highlighted that PFP@IR780@O_2 could efficiently passively target the tumor site and accurately track its distribution in vivo through self-enabled FL/PA dual-mode imaging ability, guiding specific tumors' MDT. In addition to FL/PA imaging, PFP@IR780@O_2 could also be used as a US agent due to the presence of PFP, which could undergo a liquid–gas phase transition under MW irradiation.

To investigate the US imaging potential of PFP@IR780@O_2, B-mode and CEUS imaging were conducted before and after irradiation. According to the above results, 24 h post-injection was identified as the optimal time for irradiation as the most obvious uptake of nanodroplets in tumor tissues. As shown in Figure 6D, the contrast and the corresponding echo intensity of the PFP@IR780@O_2 group on the B-mode and CEUS images enhanced after irradiation, while the LIP@IR780@O_2 and saline groups showed no obvious difference, indicating US imaging was PFP-dependent. Semi-quantification of the gray value of both US (Figure S6) and CEUS (Figure 6E) mode further confirmed these findings. These results indicate that the gas–liquid phase transition of PFP under irradiation makes PFP@IR780@O_2 capable for US imaging, providing more structure or boundary characteristics of tumors.

In vivo Monitoring of Hypoxic Tumor Conditions

With the excellent oxygen loading capacity of PFC, PFP@IR780@O_2 was expected to alleviate hypoxia in solid tumors and sustained tumor oxygenation upon treatment. Therefore, the potential anti-hypoxia capability of PFP@IR780@O_2 was investigated by utilizing in vivo PA imaging and ex vivo immunofluorescence staining. Firstly, PA imaging with the Oxy-Hemo mode was applied to monitor the oxygen supply of tumor tissues by measuring the dynamics of hemoglobin (Hb, 700 nm, represented hypoxia) and oxygenated hemoglobin (HbO_2, 850 nm, represented normoxia) in tumor tissues after different treatments. As shown in Figure 7A and B, the PFP@IR780@O_2 + MW group exhibited the highest PA signal of HbO_2 and the lowest of Hb 24 h after injection, indicating this treatment indeed alleviated hypoxia in the tumor. However, the weakest PA signal of HbO_2 and the strongest of Hb could be observed in the LIP@IR780@0_2 + MW group, implying that tumor hypoxia may be exacerbated by the sustained consumption of oxygen during therapy. Additionally, no significant statistical differences were observed in other groups. Semi-quantification of PA intensities (Figure S7) further confirmed these findings.

Afterward, tumor tissues were harvested and the ex vivo immunofluorescence staining was performed to evaluate whether the hypoxia-related signaling pathways were inhibited with hypoxia-induced factor 1 alpha (HIF-1α) protein as the endogenous indicator. Consistent with the results of PA imaging, tumors treated with PFP@IR780@O_2 showed negligible green fluorescence (Figure 7A), while other groups exhibited a higher HIF-1α level. In addition, the positive area of HIF-1α protein in the PFP@IR780@O_2 + MW group was significantly lower than that in other groups (Figure 7C), suggesting the PFP@IR780@O_2 treatment could effectively alleviate the hypoxic conditions of the tumor microenvironment while consuming oxygen to produce ROS.

To determine whether supplementation of O_2 in tumors can elevate ROS levels, a dihydroethidium (DHE) probe, which can be oxidized by intracellular ROS and produce red fluorescence, was used to stain frozen sections of tumors. Strong red fluorescence was observed in the PFP@IR780@O_2+ MW group (Figure 7A and C), confirming a high level of ROS production due to sufficient oxygen supply. These fluorescence staining results suggested that PFP@IR780@O_2 was able to increase tumorous O_2 levels upon irradiation and subsequently elevate ROS concentration for enhancing MDT.

In vivo MDT Efficiency Against Tumor

Encouraged by the above-mentioned results, tumor models of subcutaneous and orthotopic HCC were both established to investigate the in vivo therapeutic effect of PFP@IR780@O_2. Based on the in vivo biodistribution results, 24 h was selected as the optimal time point for MW irradiation (1 W/cm^2, 5 min) after tail vein injection. Tumor-bearing nude mice were randomly

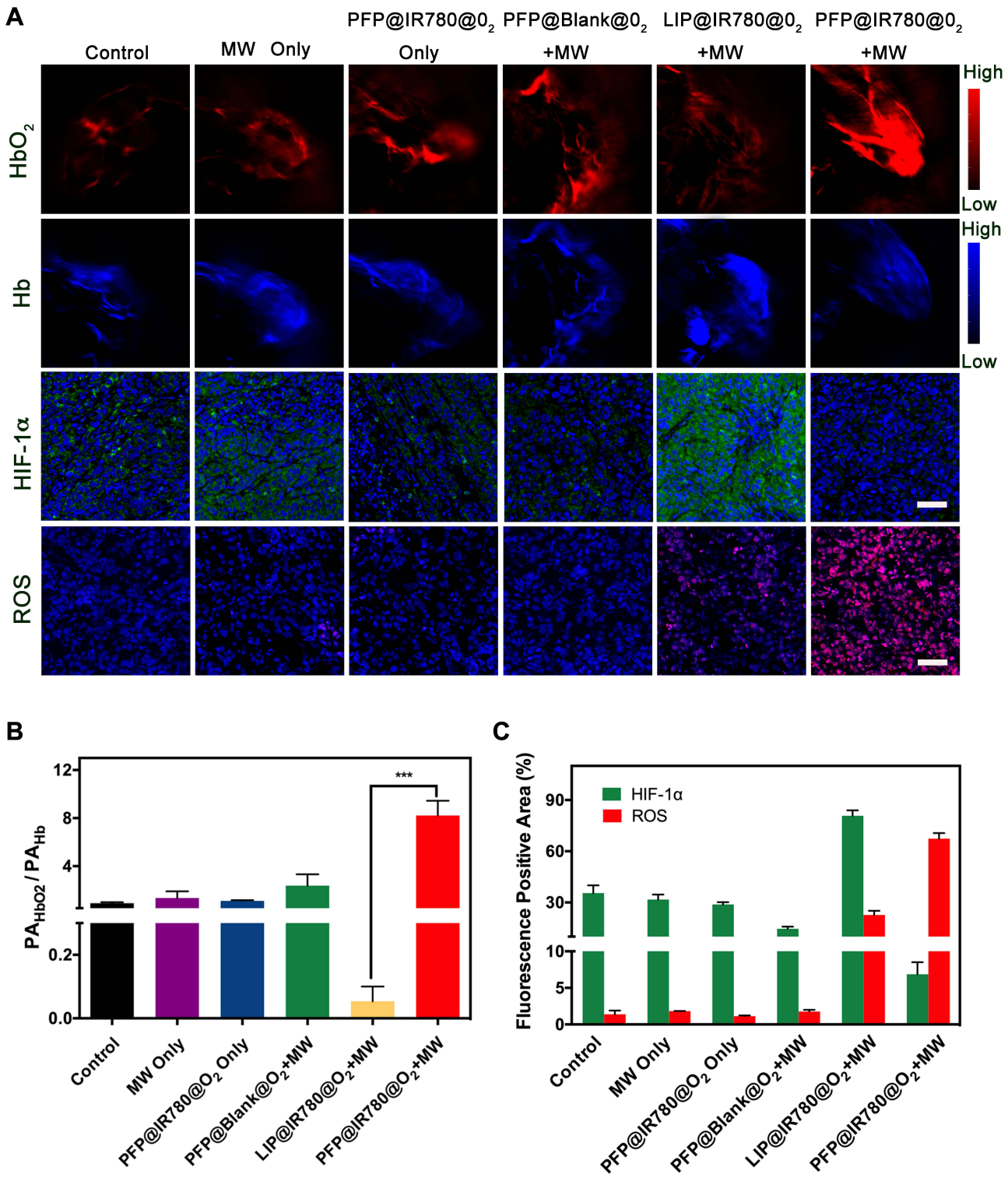

Figure 7 In vivo anti-hypoxia and ROS generation capability of PFP@IR780@O_2. (**A**) PA images, HIF-1α and ROS staining of tumor tissues after different treatments. HbO_2 (λ = 850 nm) and Hb (λ = 700 nm) monitor the real-time tumor oxygenation (the first and second line). The tumor tissue hypoxia (the third line) was determined by HIF-1α antibodies (green), while DHE (red) was used as a fluorescence indicator for ROS (the fourth line). The scale bars are 50 μm. (**B**) The ratio of HbO_2 PA intensity to Hb PA intensity. (**C**) Quantification of tumor hypoxia and ROS for different groups. Data are shown as mean ± SD. ***p < 0.001.

divided into six groups as follows: control, MW only, PFP@IR780@O_2 only, MW+PFP@Blank@O_2, MW+LIP@IR780@O_2, and MW+PFP@IR780@O_2. For the subcutaneous tumor models, the body weight and tumor volume were recorded every other day during the experiment, and the cancer therapy process was illustrated (Figure 8A). The growth status of each nude mice

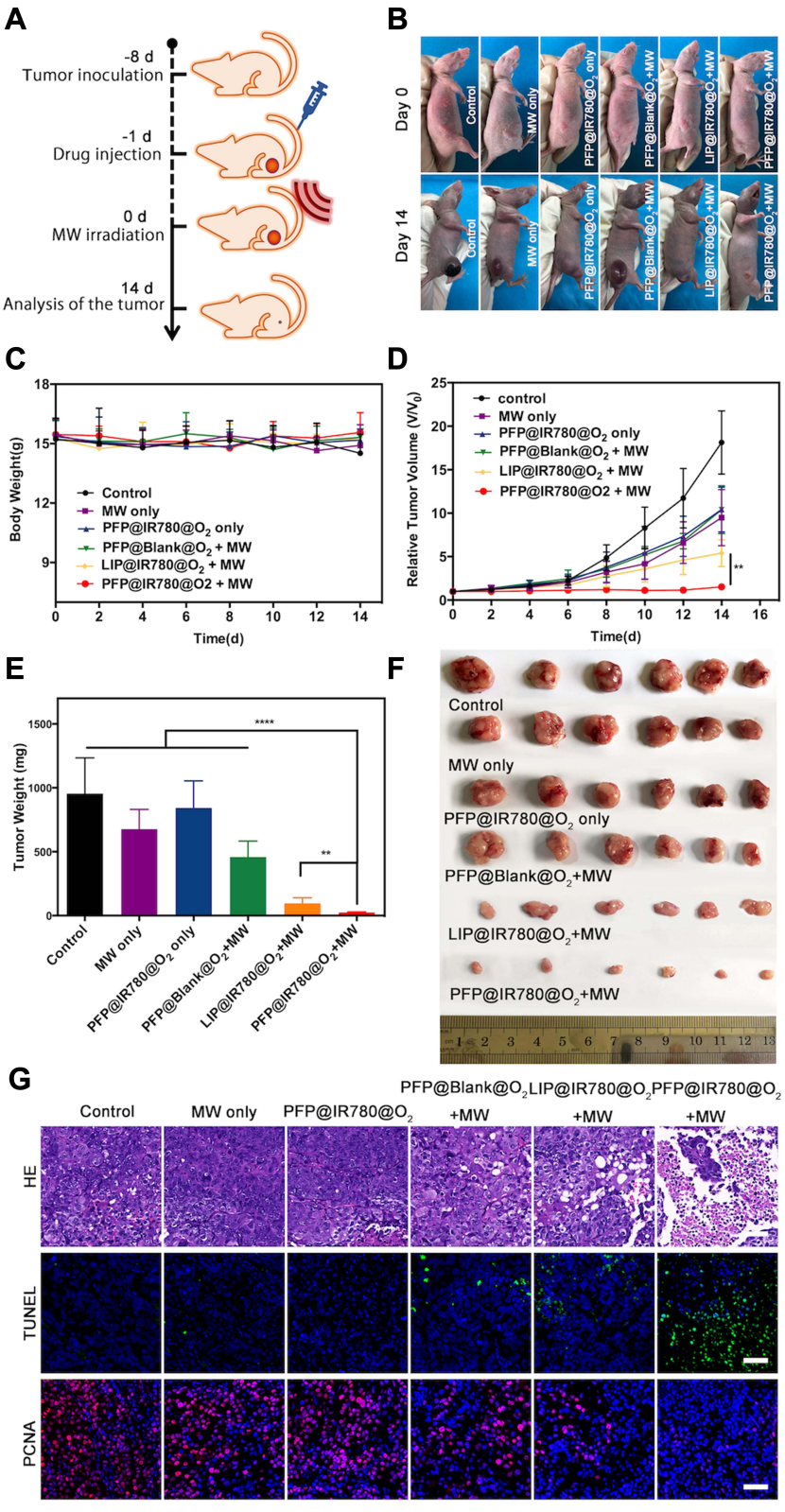

Figure 8 In vivo antitumor effect on subcutaneous tumor models (n = 6). (**A**) Schematic illustration of PFP@IR780@O_2-based tumor therapy on subcutaneous tumor models. (**B**) Representative photographs of Hepa1-6 tumor-bearing mice over a 14 day-period after various treatments. (**C**) Body weight changes of mice in the different treatments. (**D**) Tumor volume changes of the treated mice in 14 days. (**E**) The weight of excised tumors. (**F**) Photographs of tumor dissection at 14 days post treatment. (**G**) H&E, TUNEL, and PCNA staining of tumor sections after various treatments. The scale bars are 50 μm. Data are shown as mean ± SD. **p < 0.01 and ****p < 0.0001.

at the time interval of 0, 2, 4, 6, 8, 10, 12 and 14 days throughout the treatment cycle was observed (Figure 8C). It is found that the group of MW+PFP@IR780@O_2 exhibited the best inhibition of tumor growth among all six groups and almost no increase in tumor volume was observed (Figure 8B and D), while MW+LIP@IR780@O_2 demonstrated lower antitumor efficiency, suggesting the antitumor effect would be limited by tumor hypoxia. In contrast, the other groups showed rapid tumor growth with almost no therapeutic effects. Additionally, the images (Figure 8F) and weights (Figure 8E) of harvested tumors on day 14 exhibited similar trends of tumor volume changes.

Moreover, the H&E, TUNEL, and PCNA staining assays (Figure 8G) were performed to comprehensively investigate the anti-tumor effects of these treatments at a tissue level. In H&E staining, the PFP@IR780@O_2+MW group and LIP@IR780@O_2+MW group showed some necrosis-related characteristics such as cell lysis, and cytoskeleton collapse, and nuclear disintegration, but the degree of necrosis in PFP@IR780@O_2+MW group was significantly higher, indicating the best therapeutic effect. Additionally, the TUNEL assay revealed that cancer cell apoptosis induced by MDT was in line with H&E staining results, while the PCNA staining results were inconsistent, indicating a significant proliferation inhibition in the PFP@IR780@O_2+MW group. On these grounds, these staining results strongly suggested that PFP@IR780@O_2 mediated MDT could effectively induce more tumor cell apoptosis and proliferation inhibited because the enhanced tumor oxygenation enhances the MDT effect and inhibit hypoxia aggravation. It is well known that microwave produces heat for tumor ablation. The temperature changes of all the samples irradiated by microwave (1 W/cm^2, 5 min) were observed by using the infrared thermal imager and the results were exhibited in Figure S8. As shown in Figure S8, the temperature of the PFP@IR780@O_2 + MW group rose from 35.7°C to 44.9 °C, while the temperature of the control group had a similar ascending curve, but a slightly higher temperature rise (45.9 °C). Compared to the control, the self-made nanomaterials may not exhibit a significant enhancement of microwave heating effects.

For the orthotopic HCC models, the MDT effect was relatively more meaningful and the MW irradiation was performed outside of the liver but close to the tumor under ultrasound guidance. The experimental protocol is shown in Figure 9A and the growth status of tumors in each group was measured with ultrasound at the time interval of 0, 3, 6, 9, 12, and 15 days throughout the treatment (Figure 9B). Consistent with the subcutaneous tumor models results, the most distinct anticancer effect was observed in PFP@IR780@O_2+MW group, with significantly smaller sizes of tumor (Figure 9C). We also found considerably prolonged survival rate (Figure 9D), compared to all other groups.

In vivo Biosafety

The in vivo long-term biosafety of these nanoparticles after treatment was also evaluated. For both tumor models, there was no significant weight loss in the mice in each group during the treatment (Figures 8C and S9), indicating the low toxicity of these nanoparticles. For the histological analysis, H&E staining of the main organs was performed after the treatment to study the acute and chronic damage. The main organs (heart, liver, spleen, lung, kidney) of each group were completed and no tissue necrosis and metastasis were found (Figure 10A), suggesting the desirable biosafety of our nanosystem.

We further investigated a series of complete blood counts and serum biochemical indicators associated with potential organ damage. As expected, no statistical significance was observed in the levels of these liver and kidney function indicators (Figure 10B), including aminotransferase (AST), alanine aminotransferase (ALT), creatinine (CRE), and blood urea nitrogen (BUN). In addition, red blood cell (RBC), white blood cell (WBC), hemoglobin (HGB), mean red blood cell volume (MCV) and other blood routine indicators were all within the normal range.

Conclusion

In this study, the oxygen-sufficient liposomal nanoplatform was successfully prepared to effectively relieve hypoxic TME and further enhance MDT efficiency against highly aggressive HCC. Moreover, the successfully prepared nanoparticles could be also used as an efficient multimodal imaging contrast agent in vivo due to the NIR and PA imaging capabilities of IR780 and MW irradiation PFC educing US imaging. Both in vitro and in vivo experiments were conducted to demonstrate the MDT efficacy of elaborately designed nanodroplets. Therefore, this work opens a new door to treating hypoxic tumors through MW-triggered ROS-based therapy using oxygen-loaded nanoplatforms.

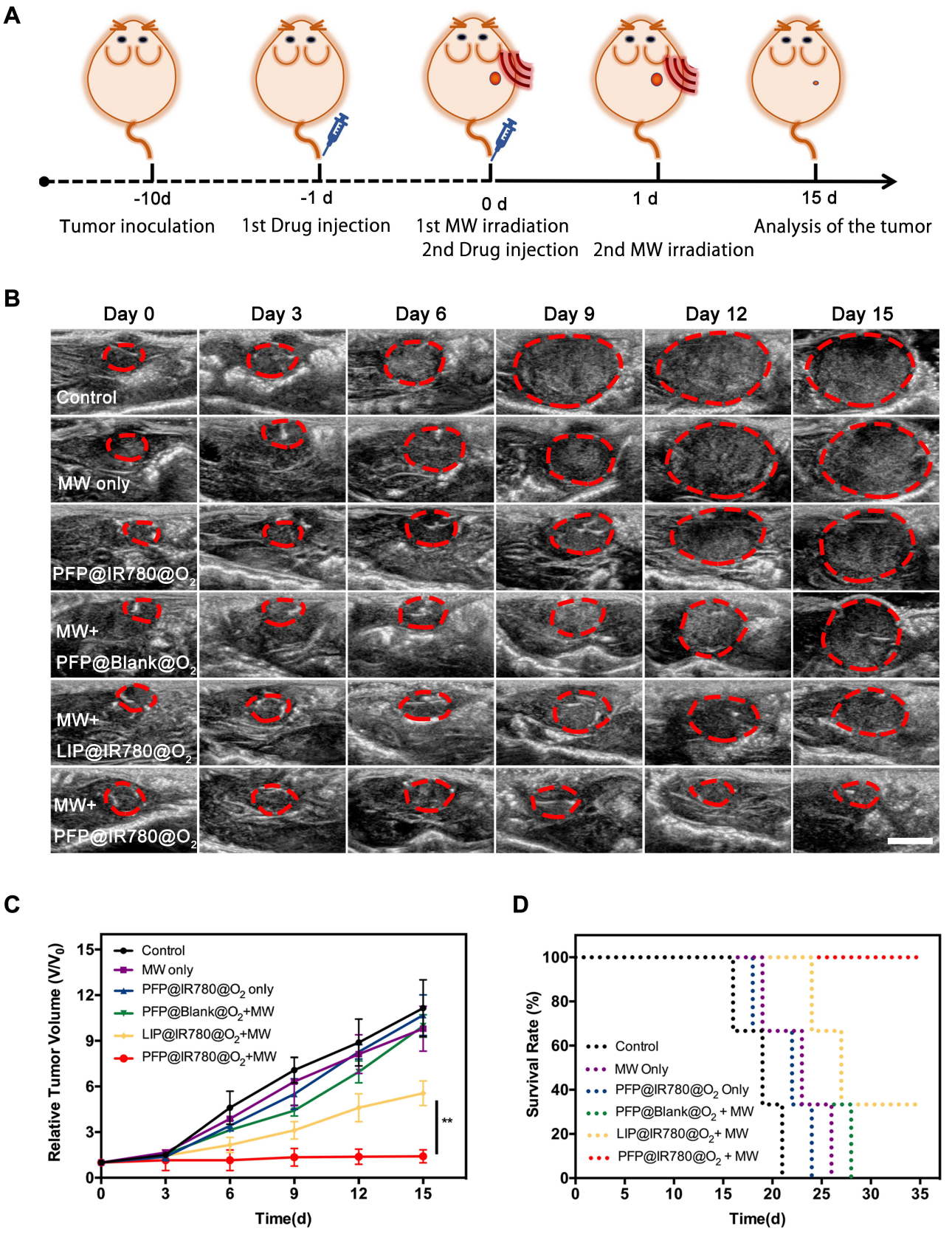

Figure 9 In vivo antitumor effect on orthotopic tumor models (n = 3). (**A**) Schematic illustration of PFP@IR780@O_2 based tumor therapy on orthotopic tumor models. (**B**) Ultrasonography surveillance of Hepa1-6 liver cancer in different treatment groups before and after treatment 3, 6, 9, 12, 15 days. The scale bars are 5 mm. (**C**) Tumor volume changes of the treated mice in 15 days. (**D**) Survival assessment of mice engrafted with orthotopic Hepa1-6 xenografts after different treatments. Data are shown as mean ± SD. **p < 0.01.

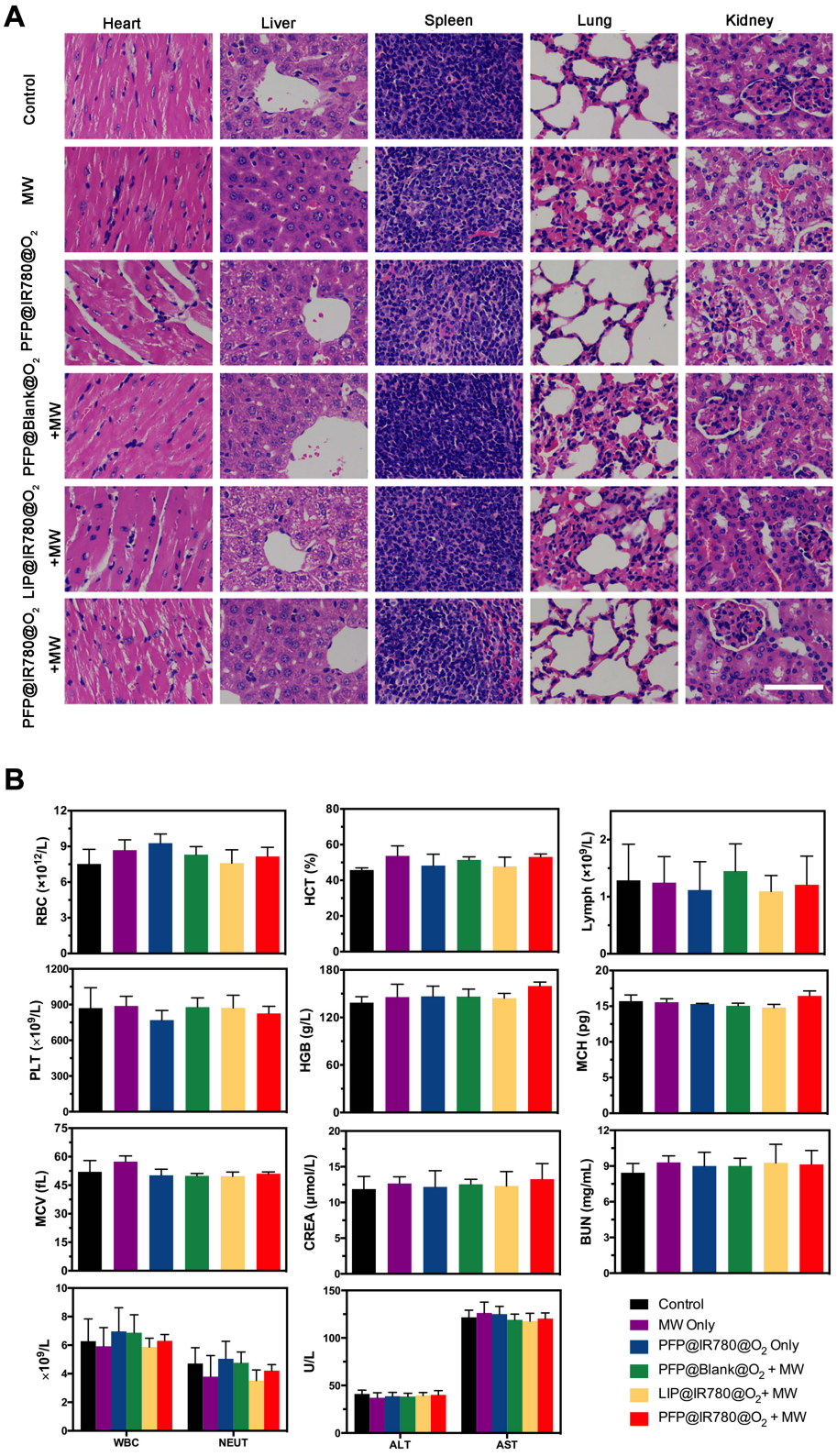

Figure 10 Biosafety analysis of different treatments in subcutaneous tumor models. (**A**) H&E staining of the major organs (heart, liver, spleen, lung, and kidney) of Hepa1-6 tumor-bearing mice after different treatments. The scale bars are 50 μm. (**B**) The changes of hematology and serum biochemical indexes including white blood cell (WBC), neutrophils (NEUT), red blood cell (RBC), hematocrit (HCT), hemoglobin (HGB), mean corpuscular volume (MCV), mean corpuscular hemoglobin (MCH), lymphocytes (Lymph), platelet (PLT), alanine aminotransferase (ALT), aspartate aminotransferase (AST), blood urea nitrogen (BUN) and serum creatinine (Crea) after different treatments. (Data are shown as mean ± SD; n = 3.).

https://doi.org/10.2147/IJN.S387223 DovePress

Acknowledgments

We greatly appreciate the financial support from the Key Program of the Science and Technology Bureau of Sichuan (No. 2022YFS0218, No. 2022NSFSC0835). The authors thank Professor Feng Yan (Laboratory of Ultrasound Imaging Drug, West China Hospital of Sichuan University, Chengdu, People's Republic of China) for his assistance. The authors are grateful to Hong Wang (Laboratory of Ultrasound Imaging Drug, West China Hospital of Sichuan University, Chengdu, People's Republic of China) and Yan Wang (Research Core Facility of West China Hospital Sichuan University) for their collaboration.

Disclosure

The authors report no conflicts of interest in this work.

References

1. Siegel RL, Miller KD, Jemal A. Cancer statistics, 2020. *CA Cancer J Clin*. 2020;70(1):7–30. doi:10.3322/caac.21590
2. Chu KF, Dupuy DE. Thermal ablation of tumours: biological mechanisms and advances in therapy. *Nat Rev Cancer*. 2014;14(3):199–208. doi:10.1038/nrc3672
3. Nault JC, Sutter O, Nahon P, Ganne-Carrie N, Seror O. Percutaneous treatment of hepatocellular carcinoma: state of the art and innovations. *J Hepatol*. 2018;68(4):783–797. doi:10.1016/j.jhep.2017.10.004
4. Fan W, Huang P, Chen X. Overcoming the achilles' heel of photodynamic therapy. *Chem Soc Rev*. 2016;45(23):6488–6519. doi:10.1039/C6CS00616G
5. Xie J, Wang Y, Choi W, et al. Overcoming barriers in photodynamic therapy harnessing nano-formulation strategies. *Chem Soc Rev*. 2021;50(16):9152–9201. doi:10.1039/d0cs01370f
6. Zhou Z, Song J, Nie L, Chen X. Reactive oxygen species generating systems meeting challenges of photodynamic cancer therapy. *Chem Soc Rev*. 2016;45(23):6597–6626. doi:10.1039/C6CS00271D
7. Chu X, Mao L, Johnson O, et al. Exploration of TiO2 nanoparticle mediated microdynamic therapy on cancer treatment. *Nanomedicine*. 2019;18:272–281. doi:10.1016/j.nano.2019.02.016
8. Fu C, Zhou H, Tan L, et al. Microwave-activated Mn-doped zirconium metal-organic framework nanocubes for highly effective combination of microwave dynamic and thermal therapies against cancer. *ACS Nano*. 2018;12(3):2201–2210. doi:10.1021/acsnano.7b08868
9. Ma X, Ren X, Guo X, et al. Multifunctional iron-based metal-organic framework as biodegradable nanozyme for microwave enhancing dynamic therapy. *Biomaterials*. 2019;214:119223. doi:10.1016/j.biomaterials.2019.119223
10. Wu Q, Xia N, Long D, et al. Dual-functional supernanoparticles with microwave dynamic therapy and microwave thermal therapy. *Nano Lett*. 2019;19(8):5277–5286. doi:10.1021/acs.nanolett.9b01735
11. Vaupel P, Mayer A. Hypoxia in cancer: significance and impact on clinical outcome. *Cancer Metastasis Rev*. 2007;26(2):225–239. doi:10.1007/s10555-007-9055-1
12. Graham K, Unger E. Overcoming tumor hypoxia as a barrier to radiotherapy, chemotherapy and immunotherapy in cancer treatment. *Int J Nanomedicine*. 2018;13:6049–6058. doi:10.2147/IJN.S140462
13. An J, Hu YG, Li C, et al. A pH/ultrasound dual-response biomimetic nanoplatform for nitric oxide gas-sonodynamic combined therapy and repeated ultrasound for relieving hypoxia. *Biomaterials*. 2020;230:119636. doi:10.1016/j.biomaterials.2019.119636
14. Wan Y, Fu LH, Li C, Lin J, Huang P. Conquering the hypoxia limitation for photodynamic therapy. *Adv Mater*. 2021;33(48):e2103978. doi:10.1002/adma.202103978
15. Sahu A, Kwon I, Tae G. Improving cancer therapy through the nanomaterials-assisted alleviation of hypoxia. *Biomaterials*. 2020;228:119578. doi:10.1016/j.biomaterials.2019.119578
16. Yang N, Xiao W, Song X, Wang W, Dong X. Recent advances in tumor microenvironment hydrogen peroxide-responsive materials for cancer photodynamic therapy. *Nanomicro Lett*. 2020;12(1):15. doi:10.3847/1538-4357/ab5f08
17. Gong L, Zhang Y, Zhao J, et al. All-in-one biomimetic nanoplatform based on hollow polydopamine nanoparticles for synergistically enhanced radiotherapy of colon cancer. *Small*. 2022;18(14):e2107656. doi:10.1002/smll.202107656
18. Wu T, Liu Y, Cao Y, Liu Z. Engineering macrophage exosome disguised biodegradable nanoplatform for enhanced sonodynamic therapy of glioblastoma. *Adv Mater*. 2022;34(15):e2110364. doi:10.1002/adma.202110364
19. Lv W, Cao M, Liu J, Hei Y, Bai J. Tumor microenvironment-responsive nanozymes achieve photothermal-enhanced multiple catalysis against tumor hypoxia. *Acta Biomater*. 2021;135:617–627. doi:10.1016/j.actbio.2021.08.015
20. Alayash AI. Mechanisms of toxicity and modulation of hemoglobin-based oxygen carriers. *Shock*. 2019;52(1SSuppl 1):41–49. doi:10.1097/SHK.0000000000001044
21. Han Z, Tu X, Qiao L, et al. Phototherapy and multimodal imaging of cancers based on perfluorocarbon nanomaterials. *J Mater Chem B*. 2021;9(34):6751–6769. doi:10.1039/D1TB00554E
22. Jägers J, Wrobeln A, Ferenz KB. Perfluorocarbon-based oxygen carriers: from physics to physiology. *Pflugers Arch*. 2021;473(2):139–150. doi:10.1007/s00424-020-02482-2
23. Krafft MP. Alleviating tumor hypoxia with perfluorocarbon-based oxygen carriers. *Curr Opin Pharmacol*. 2020;53:117–125. doi:10.1016/j.coph.2020.08.010
24. Cheng Y, Cheng H, Jiang C, et al. Perfluorocarbon nanoparticles enhance reactive oxygen levels and tumour growth inhibition in photodynamic therapy. *Nat Commun*. 2015;6:8785. doi:10.1038/ncomms9785
25. Chen J, Luo H, Liu Y, et al. Oxygen-self-produced nanoplatform for relieving hypoxia and breaking resistance to sonodynamic treatment of pancreatic cancer. *ACS Nano*. 2017;11(12):12849–12862. doi:10.1021/acsnano.7b08225
26. Balaban RS, Nemoto S, Finkel T. Mitochondria, oxidants, and aging. *Cell*. 2005;120(4):483–495. doi:10.1016/j.cell.2005.02.001

27. Hoye AT, Davoren JE, Wipf P, Fink MP, Kagan VE. Targeting mitochondria. *Acc Chem Res*. 2008;41(1):87–97. doi:10.1021/ar700135m
28. Yu Z, Sun Q, Pan W, Li N, Tang B. A near-infrared triggered nanophotosensitizer inducing domino effect on mitochondrial reactive oxygen species burst for cancer therapy. *ACS Nano*. 2015;9(11):11064–11074. doi:10.1021/acsnano.5b04501
29. An J, Hu YG, Cheng K, et al. ROS-augmented and tumor-microenvironment responsive biodegradable nanoplatform for enhancing chemo-sonodynamic therapy. *Biomaterials*. 2020;234:119761. doi:10.1016/j.biomaterials.2020.119761
30. Xu J, Chen Y, Deng L, et al. Microwave-activated nanodroplet vaporization for highly efficient tumor ablation with real-time monitoring performance. *Biomaterials*. 2016;106:264–275. doi:10.1016/j.biomaterials.2016.08.034
31. Lu KY, Lin PY, Chuang EY, et al. H2O2-depleting and O2-generating selenium nanoparticles for fluorescence imaging and photodynamic treatment of proinflammatory-activated macrophages. *ACS Appl Mater Interfaces*. 2017;9(6):5158–5172. doi:10.1021/acsami.6b15515
32. Kalyane D, Raval N, Maheshwari R, Tambe V, Kalia K, Tekade RK. Employment of enhanced permeability and retention effect (EPR): nanoparticle-based precision tools for targeting of therapeutic and diagnostic agent in cancer. *Mater Sci Eng C Mater Biol Appl*. 2019;98:1252–1276. doi:10.1016/j.msec.2019.01.066
33. Zhang E, Luo S, Tan X, Shi C. Mechanistic study of IR-780 dye as a potential tumor targeting and drug delivery agent. *Biomaterials*. 2014;35(2):771–778. doi:10.1016/j.biomaterials.2013.10.033
34. Yang Z, Wang J, Liu S, et al. Defeating relapsed and refractory malignancies through a nano-enabled mitochondria-mediated respiratory inhibition and damage pathway. *Biomaterials*. 2020;229:119580. doi:10.1016/j.biomaterials.2019.119580
35. Yu M, Xu X, Cai Y, Zou L, Shuai X. Perfluorohexane-cored nanodroplets for stimulations-responsive ultrasonography and O(2)-potentiated photodynamic therapy. *Biomaterials*. 2018;175:61–71. doi:10.1016/j.biomaterials.2018.05.019